Journal of Materials Chemistry A

ROYAL SOCIETY OF CHEMISTRY

PAPER

View Article Online
View Journal

Cite this: DOI: 10.1039/d5ta10172g

Size-dependent amorphous–crystalline phase transitions in ultra-small gold colloids

Vinavadini Ramnarain,[a] Adrien Moncomble,[a] Maxime Moreaud,[bc] Ricardo Gatti,[d] Romain Moreau,[d] Guillaume Wang,[a] Christian Ricolleau,[a] Jaysen Nelayah,[a] Nathaly Ortiz Peña,[a] Alexandre Gelabert,[e] Hakim Amara [ad] and Damien Alloyeau *[a]

Understanding the atomic-scale mechanisms governing the structural evolution of ultra-small metal nanoparticles (NPs) is critical for controlling their synthesis and properties in catalysis and nanomedicine. Using aberration-corrected high-resolution transmission electron microscopy in graphene liquid cells, we investigated the dynamics of ultra-small gold colloids at the atomic scale during their growth by Ostwald ripening. This slow coarsening process in which atoms flux between NPs can make them grow or shrink allows us to shed new light on the size-dependent amorphous–crystalline phase transition in gold colloids. Indeed, NPs larger than 2.3 nm are crystalline, while NPs smaller than 1.7 nm are always amorphous. Interestingly, the phase transition between these two phases is systematically observed between 1.7 and 2.3 nm, both during the growth and the dissolution of NPs. The reversibility of this transition suggests a size-dependent equilibrium between amorphous and crystalline phases that is confirmed by Monte Carlo simulations performed within a tight-binding framework. Beyond offering quantitative insights into the phase diagrams of ligand-free gold colloids, these *in situ* observations provide mechanistic insights into the formation of monocrystalline nanostructures that could help rationalize the growth control of metal NPs.

Received 12th December 2025
Accepted 7th March 2026

DOI: 10.1039/d5ta10172g

rsc.li/materials-a

1. Introduction

Understanding the atomic-scale mechanisms involved in the nucleation, growth and etching of ultra-small metal nanoparticles (NPs) is essential for generating new concepts and protocols in nanochemistry. Moreover, given their wide applications in medicine and catalysis,[1,2] deciphering the structural dynamics of metal colloids in the 0.5- to 3-nm range is also crucial for developing efficient nanotechnologies. In this context, liquid-phase transmission electron microscopy (LPTEM) has opened the possibility of visualizing the formation processes of metal NPs, providing mechanistic information inaccessible to ensemble measurements (absorption spectroscopy, X-ray scattering, *etc.*).[3–6] Remarkably, atomic-scale LPTEM investigations revealed that the nucleation mechanisms of metal NPs[7–9] and nanoalloys[10] go through an amorphous phase-mediated crystallization. This two-step process involves the formation and growth by coalescence of amorphous nanoclusters in which crystallization occurs when the amorphous nanostructures reach a size of a few nanometers. When stabilized by specific ligands, the coalescence of "magic number" clusters can be involved in the growth of the intermediate amorphous Au NPs.[11] Therefore, the phase transformation of ultra-small NPs from an amorphous to a crystalline state is the key step in controlling the structure of the first crystalline seeds formed in solution, which impacts the growth mechanisms and the final shape of NPs. However, given the difficulty in monitoring the dynamics of ultra-small NPs, the many kinetic and thermodynamic factors that dictate this phase transition, especially the effects of NP size, remain poorly understood, preventing the fine control of the crystallization pathways.[12] One way of determining whether the amorphous phase of ultra-small NPs corresponds to a size-dependent thermodynamic equilibrium or to a non-equilibrium structure due to rapid nucleation and growth processes would be to detect the same phase transition during NP dissolution. So far, LPTEM has been exploited to reveal the role of reaction kinetics, defects, and functionalization on the etching mechanisms of metal nanoparticles.[13,14] However, amorphous intermediates in the very last steps of ultra-small NP dissolution have never been demonstrated.

Computational methods have also been deeply employed to determine the structural stability of ultra-small gold

[a]Université Paris Cité, CNRS, Laboratoire Matériaux et Phénomènes Quantiques, 75013 Paris, France. E-mail: damien.alloyeau@u-paris.fr
[b]Manufacture Française des Pneumatiques Michelin, 63000 Clermont-Ferrand, France
[c]IFP Énergies Nouvelles, 69360 Solaize, France
[d]Université Paris-Saclay, ONERA, CNRS, Laboratoire d'Etude des Microstructures, 92322 Chatillon, France
[e]Aix-Marseille Université, CNRS, IRD, INRAE, CEREGE, 13545 Aix-en-Provence, France

nanoparticles. Using semi-empirical and first-principles approaches to describe the bonding in gold nanoclusters, Garzón and co-workers found essentially equal structural stability for amorphous and crystalline isomers of Au_n ($n = 38$, 55, 75) clusters with sizes in the range of 1–1.5 nm.[15] Molecular dynamics simulations using the Gupta potential also revealed very small energy differences (below 0.001 eV per atom) between Au_{38} clusters with amorphous, Face-Centred Cubic (FCC) and icosahedral structures up to room temperature.[16] Given the degenerate state of these amorphous and crystalline isomers, conflicting results are found in the literature about the effects of NP size on their thermodynamic equilibrium, since the most stable structure is highly affected by the employed potential and simulation protocol.[17] Therefore, combining experimental and theoretical approaches is a way to obtain unambiguous results regarding the phase diagram of ultra-small gold colloids.

Here, we exploit the outstanding temporal and spatial resolutions of aberration-corrected high-resolution transmission electron microscopy (HRTEM) in graphene liquid cells (GLCs) and Monte Carlo (MC) simulations performed within a tight-binding framework to shed new light on the size dependency and reversibility of the amorphous–crystalline phase transition in ultra-small gold colloids.

2. Results and discussion

GLCs containing an aqueous solution of $HAuCl_4$ were analysed by TEM (see the Experimental section for details). The very first second of observation at low and medium magnifications generates the nucleation of gold NPs *via* beam-induced water radiolysis (Fig. 1a). As described in many liquid-phase TEM studies,[18,19] the products of water radiolysis include strong reducing agents, namely aqueous electrons and hydrogen radicals, that reduce metal precursors and generate the nucleation and growth of nanocrystals by monomer attachment. However, as graphene liquid pockets do not allow the injection of precursor solutions during TEM observations, the concentration of precursors decreases rapidly, and the continuous

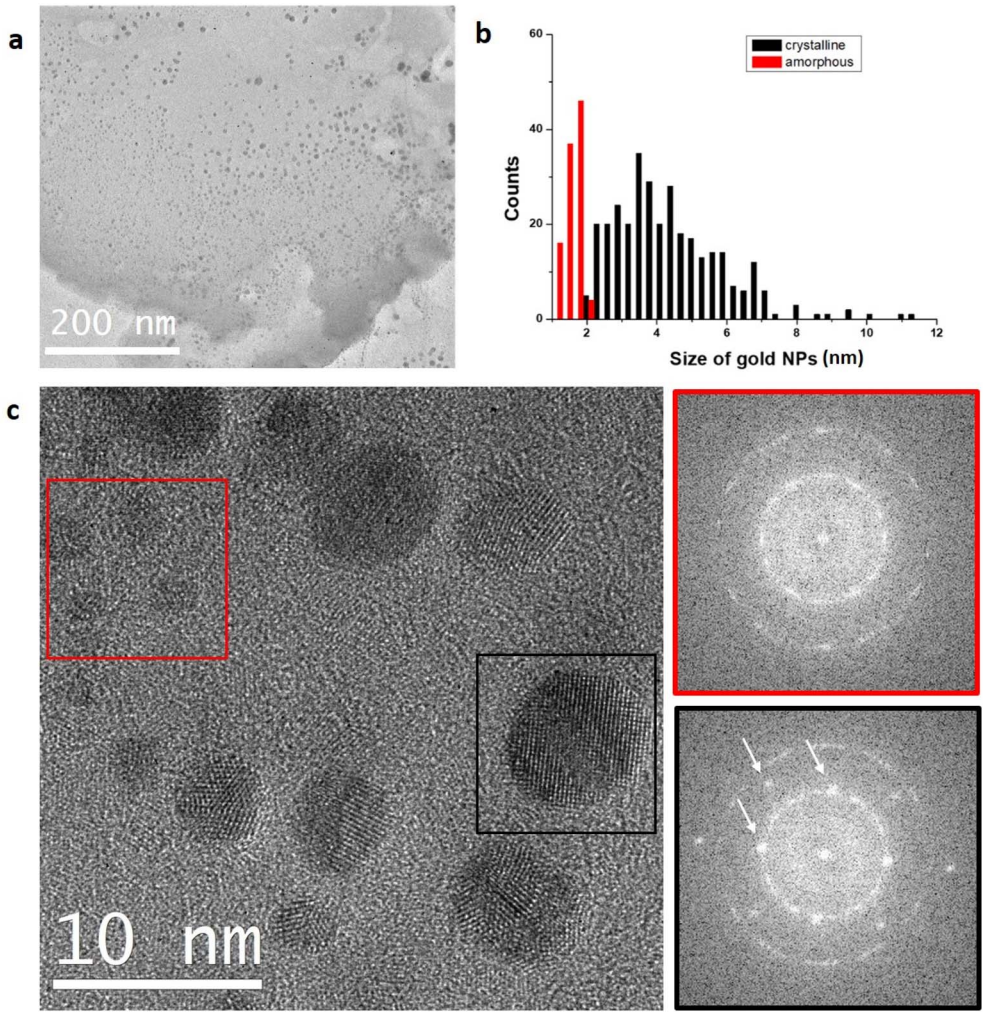

Fig. 1 (a) Low magnification TEM image of a graphene liquid pocket just after the nucleation burst of gold NPs. (b) Size distribution of amorphous clusters in red and crystalline NPs in black. (c) HRTEM image of crystalline NPs (black square) and amorphous clusters (red square) in a GLC. The Fourier transforms on the right show that only the signal of multilayer graphene is detected in the red area, where several amorphous clusters are observed, while the signal of the gold lattice (indicated by white arrows) is seen in the black area.

growth of all the NPs in the irradiated area, which is a characteristic of radiolysis-driven formation processes, is no longer observed after a few seconds. By measuring the density (~1000 NPs per μm^2) and the mean size (3.1 nm) of NPs formed after this nucleation and growth phase driven by radiolysis, one can estimate the total amount of gold atoms in the NPs. By comparing this amount of gold in the metallic state with the amount of gold precursor molecules before irradiation in the liquid pockets, whose volume is estimated using low magnification images ($\sim 10^8$ nm^3 for the pocket seen in Fig. 1a), we can deduce that the vast majority of gold precursors have been reduced in the early stages of this experiment. Consequently, in the subsequent HRTEM analyses, the absence of radiolytic growth allows studying coarsening processes mainly driven by Ostwald ripening (OR). This key process in the synthesis and the life-cycle of nanoparticles in their application media affects their size distribution through the dissolution of smaller nanostructures that redeposit onto the larger ones, due to differences in chemical potential.[20–22] Many *in situ* TEM studies in liquid or on substrates allowed quantifying the atomic exchanges between NPs during OR.[23–26] As illustrated in Video V1 in the SI, neighbouring NPs constantly exchange atoms with each other, leading to a continuous restructuring of their surfaces and a synchronized variation of their size. Thus, OR induces slow growth of the stable NPs at the expense of the ones that slowly dissolve in the solution until they disappear. Such conditions where OR dominates the dynamics of colloids are here used to explore size effects on the phase diagram of nanostructures, since phase transitions can be observed during NP growth and etching.

Fig. 1c shows that two types of Au NPs are found in the GLCs after the main nucleation phase, namely small spherical amorphous clusters and larger crystalline NPs. Obviously, amorphous objects cannot generate diffraction contrast in HRTEM images. Therefore, the only peaks observed in the Fourier transform of areas containing only amorphous NPs (red square in Fig. 1c) come from the interaction of the beam with the graphene layers. However, given the differences in scattering strength, projected electrostatic potential and mass density between the gold NPs and the GLCs, amorphous gold

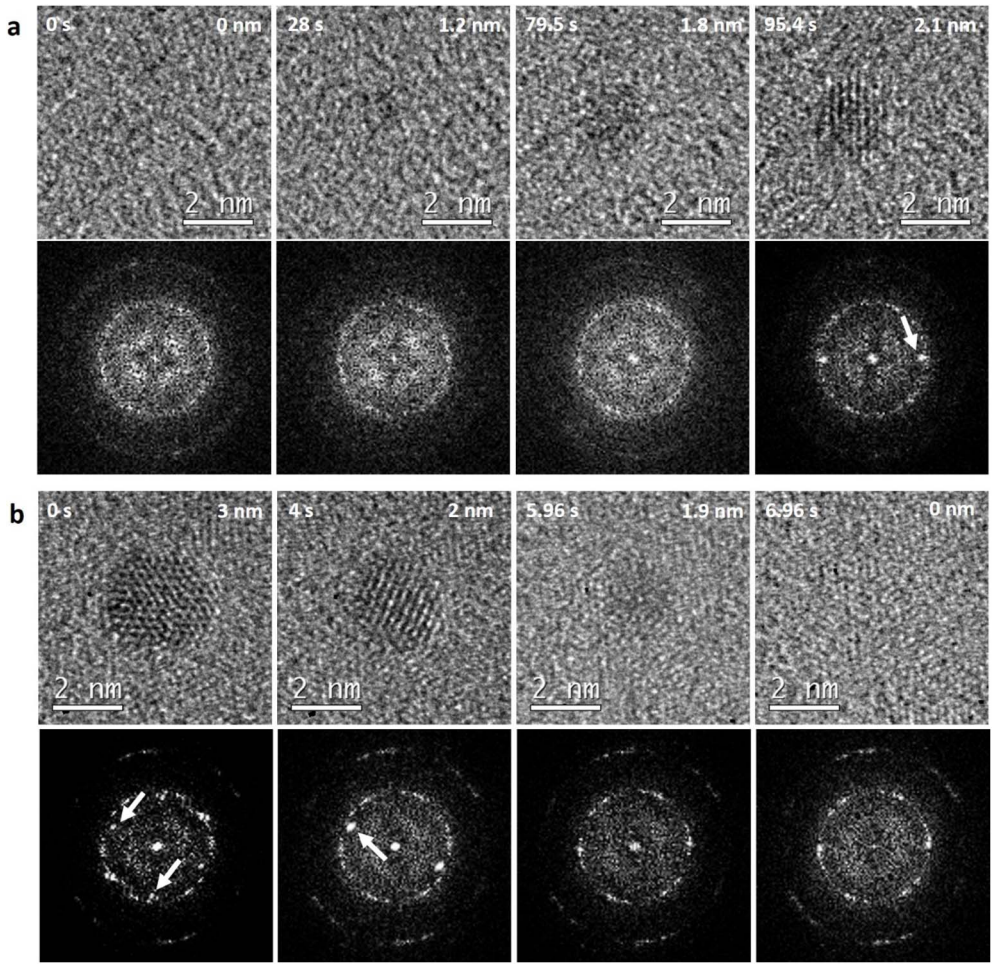

Fig. 2 HRTEM image series with the corresponding Fourier transform below each image, on which the signal of the gold lattice is indicated by white arrows. The acquisition time and the size of the observed NPs are indicated in the top left and right corners of HRTEM images, respectively. (a) Nucleation and growth by monomer attachments of an amorphous cluster that crystallizes when its size reaches 2.1 nm (see associated Video V2 in SI). (b) Complete isotropic etching of a truncated octahedron that loses its crystallinity when its size reaches 1.9 nm (see associated Video V3 in SI).

NPs also generate mass–thickness and phase contrasts, which make them darker than the background.[27] As illustrated in Fig. S1, these two contrast formation mechanisms result in a significant reduction in the signal from amorphous NPs, with a clear intensity transition at the edges, allowing their size to be measured accurately (±0.2 nm). As seen in Fig. 1b, amorphous clusters present a Gaussian size distribution ranging from 0.8 nm to 2.3 nm, while crystalline NPs have a broader size distribution between 1.7 nm and 12 nm. These HRTEM analyses reveal a clear correlation between the size and the structure of gold NPs, with a slight overlap in the size distributions of the two NP populations. Phase transitions between these two structural configurations were studied during the dynamic observations of OR processes at the atomic scale. As illustrated in Fig. 2a and associated Video V2 in the SI, the nucleation of amorphous gold clusters has been recorded very occasionally during the coarsening of the NP assembly. Due to OR, some amorphous clusters grow isotropically by monomer attachment, but they always remain spherical and amorphous up to a diameter of 1.7 nm. Structural analyses in the real and Fourier spaces show that crystallization systematically occurs when clusters reach a size between 1.7 and 2.3 nm, leading to the formation of monocrystalline NPs with a truncated octahedron shape. Once above 2.3 nm, NPs remain crystalline and keep evolving in size *via* OR. Remarkably, the inverse phase transition is observed in the same size range during the dissolution of NPs (Fig. 2b and Video V3 in the SI). Indeed, under isotropic etching, monocrystalline NPs retain their crystal structure up to a size of 2.3 nm. Then, their amorphization occurs in a size range between 2.3 and 1.7 nm before complete dissolution. Fast HRTEM imaging reveals that between 1.7 and 2.3 nm, NPs can transition several times from one phase to another (Fig. 3 and the Videos V2–V4 in the SI), which indicates that both amorphous and crystalline structures are stable in this size range.

The loss of atomic contrasts in HRTEM images could possibly be due to the rotation of NPs that could place them under orientation conditions where no Bragg peak can be detected on the FFT of HRTEM images. By simulating one thousand HRTEM images of a 1.5 nm cuboctahedral gold NP with random orientations (see the Experimental section and Fig. S2), we show that such orientation conditions where a crystalline NP appears amorphous on an aberration-corrected TEM image are observed in only 4% of the images. The narrowness of the angular range in which the NPs are completely out of Bragg conditions and the very slow motion of NPs in GLCs due to their strong interaction with the graphene, make a misinterpretation of their structure due to their rotation very unlikely. Moreover, during the crystallization and the amorphization of monocrystalline NPs, both amorphous and crystalline areas are frequently observed within the same NPs (Fig. S3). The detection of such intermediate states confirms that *in situ* HRTEM monitoring can indeed capture the dynamics of phase transitions in ultra-small metal colloids. To fully understand this last statement, we suggest watching Videos V3 and V4 in slow motion to see the many transitions between the amorphous and crystalline phases when the NPs reach the biphasic size domain and the intermediate states captured during the phase transitions.

To investigate the impact of the NP size on the relative stability of crystalline and amorphous structures, MC simulations at the atomic scale were performed (see the Experimental section for details). More precisely, cuboctahedral NPs ranging in size from 1 to 4 nm are considered in vacuum. Amorphous structures have been obtained after heating the NPs beyond the melting point and quenching them at a low temperature to reach an equilibrium configuration. Since amorphous structures are not unique, ten configurations were considered for each size. As seen in Fig. 4, between 1 and 1.5 nm, the energy differences between the two phases are below kT, corresponding to a structural bistability. When the NP size increases, the competition between the different amorphous and crystalline phases evolves significantly in favor of a more stable crystalline structure. From 2 nm, the energy difference is significant (around 75 meV per at), clearly indicating that large NPs tend to

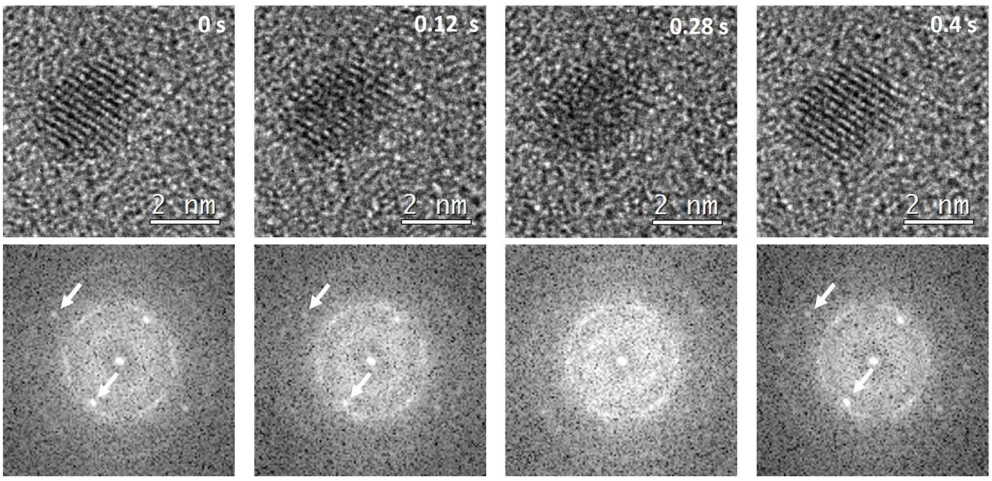

Fig. 3 Ultra-fast amorphization and recrystallization of a 2.3 nm gold NP under etching. HRTEM image series with the corresponding Fourier transform below each image, on which the signal of the gold lattice is indicated by white arrows. The acquisition time is indicated in the top right corner of HRTEM images (see associated Video V4 in SI).

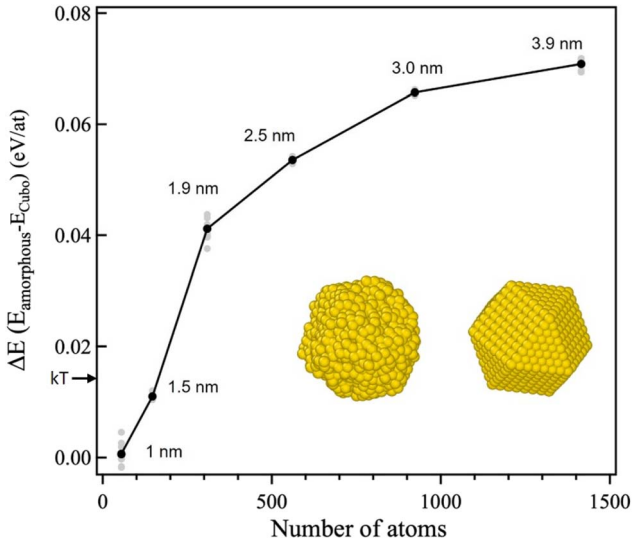

Fig. 4 Monte Carlo simulations performed within a tight-binding framework at 150 K showing the total energy difference between 10 amorphous NPs and a FCC monocrystalline nanocrystal as a function of the number of atoms. The grey dots correspond to the energy differences calculated for each amorphous NP and the black dot is to the average total energy of all the amorphous configurations. The corresponding size of the NP is indicated next to each data point. The 3D representations of an amorphous and a cuboctahedral NP extracted from the Monte Carlo simulations are shown in the inset.

preferentially adopt a crystalline structure. Therefore, these atomistic simulations confirm the size effects evidenced experimentally on the atomic structure of ultra-small NPs. The slight discrepancies between our experimental and theoretical results regarding the size range of the biphasic regime are most likely due to electron beam irradiation that can destabilize nanocrystal structures and slightly increase the size range in which the phase transition occurs. Indeed, several *ex situ* high resolution (S)TEM studies have demonstrated that the structure of ultra-small ligand free gold NPs fabricated on amorphous carbon by a vapor phase deposition technique is unstable under electron beam irradiation.[28–31] In line with the many local energy minima predicted by atomistic simulations, gold NPs with a size below 2 nm, exhibit various structural configurations ranging from icosahedron, decahedron, FCC, octahedron to amorphous but beam-induced surface diffusion and even structural fluctuations from one configuration to another have been systematically observed. In vacuum, knock-on damage and relaxation of collective electronic (plasmon) excitations possibly contribute to the structural instability of clusters under the electron beam.[32,33] In liquid, on the one hand, the radiolysis of the solvent affects the chemical environment of the NPs (pH and redox potential), which can also influence their structural configuration through surface reaction mechanisms.[19] On the other hand, the high thermal conductivity of both water and graphene reduces the beam induced temperature increase of the GLCs way below the melting temperature of gold clusters.[18,34,35] Thus, while thermal effects can be neglected, considering energy transfers from the beam to the NPs through ballistic effects or inelastic scattering phenomena, as well as the influence of radiolysis on the local environment of the NPs, remains essential to reduce the gap between *in situ* TEM investigations and atomistic simulations of ultra-small colloid structural properties.

3. Conclusion

In this study, we have demonstrated that the atomic structure of ligand-free gold colloids is strongly governed by the NP size. By studying the growth of gold NPs induced by Ostwald ripening by using aberration-corrected HRTEM in GLCs, we revealed that gold NPs below 1.7 nm are systematically amorphous, while those above 2.3 nm are always crystalline. Most importantly, we observed a reversible amorphous–crystalline phase transition within the critical size range of 1.7–2.3 nm during both growth and dissolution. This quantitative information on the nano-phase diagram of gold colloids is confirmed by atomistic simulations. The reversibility of this phase transition and the good agreement between the experimental and theoretical results provide direct evidence of a size-dependent thermodynamic equilibrium between amorphous and crystalline states and rule out the kinetic stabilization of ultra-small amorphous gold NPs. Interestingly, this intrinsic structural property of gold nanocrystals could explain the sharp size threshold around 2 nm in the catalytic activity of gold nanoparticles that has been reported for several reactions.[36,37]

Furthermore, these *in situ* TEM observations also provide the opportunity to evaluate the impact of the nucleation and growth pathways on the final structure of NPs. Indeed, although the coalescence of nanocrystals was occasionally observed long after their crystallization (see Video V5 in the SI), it is worth noting that the coalescence of amorphous clusters was never detected, even when several clusters are very close to each other (see Video V2 in the SI). By comparing our observations with the study by Jin *et al.*,[11] where amorphous cluster growth was driven by coalescence leading to the formation of polycrystalline NPs, we can assume that slow growth by monomer attachment of amorphous clusters favours the crystallization of monocrystalline NPs. Altogether, these results provide a better understanding of both the size-dependent phase diagram and formation pathway of ultra-small gold colloids that can help rationalize their synthesis and explain their performance in catalysis. As seed-mediated synthesis is a very powerful and popular method to control the shape of metal nanoparticles,[38] one of the most interesting avenues opened up by our study would be to investigate the effects of ligands commonly used to control the size and shape of gold seeds, such as cationic surfactants, citrates or thiols,[39,40] on the amorphous–crystalline phase transition and OR processes.

4. Experimental section

4.1 *In situ* HRTEM imaging in GLCs

A stock solution of 10 mM gold(III) chloride trihydrate was prepared to be encapsulated within the GLCs. The chemicals were purchased from Sigma-Aldrich and used as received. The GLCs were assembled using a Naiad-1 system from VitroTEM.

The latter enabled the automation of GLC assembly in less than ten minutes, and moreover, 5 liquid cells could be prepared simultaneously. The grids were first placed in the flow cell and etched for 5 hours. The TEM grid is placed on the grid carrier together with blotting paper. 1 μL of gold precursor solution is placed on the grid, and graphene is then automatically deposited by the Naiad system *via* the transfer loop placed on the loop carrier. The equipment comprised an etching solution, a buffer solution, ethanol, water, a loop cartridge, a disk carrier and TEM grids. A single layer of graphene was deposited on the TEM grids to have an optimal resolution during the experiment. After assembly, the GLCs were ready immediately to be examined under the microscope.

The gold NP dynamics was probed in real time using an aberration-corrected JEOL ARM 200F equipped with a cold-FEG. High resolution TEM imaging was performed at 80 kV in continuous capture mode (25 frames per second) with a One-View camera from Gatan. Upon the assembly of the GLCs, liquid pockets are formed in several areas, within which the formation and growth of gold NPs take place. These pockets (1–2 microns) are inspected first at a lower magnification and then zoomed in at the atomic scale to examine the growth of NPs by OR. HRTEM imaging was carried out at an electron dose rate of 3×10^5 electrons A^{-2} s^{-1}.

4.2 Atomic-scale simulations

We performed MC simulations in the canonical ensemble and based on the Metropolis algorithm according to a Boltzmann type probability distribution to relax the structures.[41] The Au–Au interaction is modeled by a N-body potential derived from the second moment approximation (SMA) of the tight-binding (TB) scheme.[42] This approach is particularly well adapted for transition and noble metals, where cohesive properties are driven by the d-electron band. Regarding the TB-SMA potential more details can be found in ref. 43 which illustrates the transferability of the potential. The atomic interaction potential in implemented in a MC code using the open source Large-scale Atomic/Molecular Massively Parallel Simulators (LAMMPS) package.[44] In the canonical ensemble, the MC procedure consists of a series of cycles in which random displacement moves of Au atoms are attempted and correspond to a series of macro-steps. Each macro-step randomly performs displacement moves for Au atoms. Typical runs consist of 10^3 external MC loops, each of them randomly performing 10^3 atomic displacement trials. This number of macro-steps is large enough to reach the equilibrium state. Lastly, the average quantities are computed over the second half of the final MC steps. Concerning the amorphous structures, they have been obtained by performing simulated annealing. In this process, the ordered structures are heated to 1000 K, above the melting temperature, to generate amorphous configurations. These are then cooled down to 5 K to obtain fully relaxed structures.

4.3 Multi-slice HRTEM image simulations

Simulated HRTEM images were computed based on dynamical theory using the Dr. Probe software package[45] and the multi-slice method.[46] This software was chosen due to its compatibility with scripting languages such as Python, which streamlines the process of generating large volumes of images. All simulation parameters are listed in Table S1 in the SI and correspond to the optical parameters of the double aberration-corrected JEOL ARM200F electron microscope.

Author contributions

Vinavadini Ramnarain (formal analysis: equal; investigation: equal; writing – original draft: equal); Adrien Moncomble (investigation: supporting); Ricardo Gatti (writing – review & editing: supporting); Romain Moreau (investigation: supporting); Guillaume Wang (investigation: supporting); Christian Ricolleau (writing – review & editing: supporting); Jaysen Nelayah (writing – review & editing: supporting); Nathaly Ortiz-Peña (writing – review & editing: supporting); Alexandre Gelabert (funding acquisition: equal; writing – review & editing: supporting); Hakim Amara (investigation: lead; methodology: lead; software: lead; writing – original draft: supporting; writing – review & editing: supporting); Damien Alloyeau (conceptualization: lead; formal analysis: lead; funding acquisition: equal; investigation: lead; methodology: lead; project administration: lead; resources: lead; supervision: lead; writing – original draft: lead; writing – review & editing: lead).

Conflicts of interest

There are no conflicts of interest to declare.

Data availability

All the data relevant for this study are available from the corresponding author upon reasonable request by email.

Supplementary information (SI): additional figures and videos supporting the findings of this study. See DOI: https://doi.org/10.1039/d5ta10172g.

Acknowledgements

We gratefully acknowledge the financial support of the Region Ile-de-France (convention SESAME E1845 for the JEOL ARM 200F electron microscope installed at the Université Paris Cité), the French National Research Agency (ANR Project MAMBA), the labex SEAM and the Idex Université Paris Cité.

References

1 K. An and G. A. Somorjai, *ChemCatChem*, 2012, **4**, 1512–1524.
2 X. Jiang, B. Du, Y. Huang and J. Zheng, *Nano Today*, 2018, **21**, 106–125.
3 D. Alloyeau, N. Ortiz Pena, G. Wang, C. Ricolleau and J. Nelayah, *Adv. Phys.:X*, 2025, **10**, 2481277.
4 B. H. Kim, J. Yang, D. Lee, B. K. Choi, T. Hyeon and J. Park, *Adv. Mater.*, 2018, **30**, 1703316.
5 T. J. Woehl, *Chem. Mater.*, 2020, **32**, 7569–7581.

6 A. Khelfa, J. Nelayah, H. Amara, G. Wang, C. Ricolleau and D. Alloyeau, *Adv. Mater.*, 2021, **33**, 2102514.
7 W. Dachraoui and R. Erni, *Chem. Mater.*, 2023, **35**, 1201–1208.
8 J. Yang, J. Koo, S. Kim, S. Jeon, B. K. Choi, S. Kwon, J. Kim, B. H. Kim, W. C. Lee, W. B. Lee, H. Lee, T. Hyeon, P. Ercius and J. Park, *J. Am. Chem. Soc.*, 2019, **141**, 763–768.
9 N. D. Loh, S. Sen, M. Bosman, S. F. Tan, J. Zhong, C. A. Nijhuis, P. Kral, P. Matsudaira and U. Mirsaidov, *Nat. Chem.*, 2017, **9**, 77–82.
10 W. Dachraoui, M. I. Bodnarchuk and R. Erni, *ACS Nano*, 2022, **16**, 14198–14209.
11 B. Jin, Y. Wang, C. Jin, J. J. De Yoreo and R. Tang, *J. Phys. Chem. Lett.*, 2021, **12**, 5938–5943.
12 J. De Yoreo, *Nat. Mater.*, 2013, **12**, 284–285.
13 M. Sun, J. Tian and Q. Chen, *Ultramicroscopy*, 2021, **231**, 113271.
14 A. Khelfa, J. Meng, C. Byun, G. Wang, J. Nelayah, C. Ricolleau, H. Amara, H. Guesmi and D. Alloyeau, *Nanoscale*, 2020, **12**, 22658–22667.
15 I. L. Garzón, K. Michaelian, M. R. Beltrán, A. Posada-Amarillas, P. Ordejón, E. Artacho, D. Sánchez-Portal and J. M. Soler, *Phys. Rev. Lett.*, 1998, **81**, 1600–1603.
16 I. Garzón, K. Michaelian, M. Beltrán, A. Posada-Amarillas, P. Ordejón, E. Artacho, D. Sánchez-Portal and J. Soler, *Eur. Phys. J. D*, 1999, **9**, 211–215.
17 Y. Y. Gafner, Z. V. Goloven'ko and S. Gafner, *J. Exp. Theor. Phys.*, 2013, **116**, 252–265.
18 B. Fritsch, S. Lee, A. Körner, N. M. Schneider, F. M. Ross and A. Hutzler, *Adv. Mater.*, 2025, **37**, 2415728.
19 T. J. Woehl and P. Abellan, *J. Microsc.*, 2017, **265**, 135–147.
20 I. M. Lifshitz and V. V. Slyozov, *J. Phys. Chem. Solids*, 1961, **19**, 35–50.
21 C. T. Campbell, *Surf. Sci. Rep.*, 1997, **27**, 1–111.
22 M. Kahlweit, *Adv. Colloid Interface Sci.*, 1975, **5**, 1–35.
23 D. Alloyeau, T. Oikawa, J. Nelayah, G. Wang and C. Ricolleau, *Appl. Phys. Lett.*, 2012, **101**, 121920.
24 D. Alloyeau, G. Prévot, Y. Le Bouar, T. Oikawa, C. Langlois, A. Loiseau and C. Ricolleau, *Phys. Rev. Lett.*, 2010, **105**, 255901.
25 G. Prévot, N. T. Nguyen, D. Alloyeau, C. Ricolleau and J. Nelayah, *ACS Nano*, 2016, **10**, 4127–4133.
26 H. L. Xin and H. Zheng, *Nano Lett.*, 2012, **12**, 1470–1474.
27 J. C. Spence, *High-Resolution Electron Microscopy*, OUP Oxford, 2013.
28 S. Iijima and T. Ichihashi, *Phys. Rev. Lett.*, 1986, **56**, 616–619.
29 Z. Y. Li, N. P. Young, M. Di Vece, S. Palomba, R. E. Palmer, A. L. Bleloch, B. C. Curley, R. L. Johnston, J. Jiang and J. Yuan, *Nature*, 2008, **451**, 46–48.
30 Z. W. Wang and R. E. Palmer, *Nano Lett.*, 2012, **12**, 5510–5514.
31 Z. W. Wang and R. E. Palmer, *Phys. Rev. Lett.*, 2012, **108**, 245502.
32 D. Knez, M. Schnedlitz, M. Lasserus, A. Schiffmann, W. E. Ernst and F. Hofer, *Ultramicroscopy*, 2018, **192**, 69–79.
33 A. V. Verkhovtsev, Y. Erofeev and A. V. Solov'yov, *Phys. Rev. B*, 2023, **108**, 115423.
34 M. Rapacioli, N. Tarrat and F. Spiegelman, *J. Phys. Chem. A*, 2018, **122**, 4092–4098.
35 A. Chmielewski, J. Nelayah, H. Amara, J. Creuze, D. Alloyeau, G. Wang and C. Ricolleau, *Phys. Rev. Lett.*, 2018, **120**, 025901.
36 M. Turner, V. B. Golovko, O. P. H. Vaughan, P. Abdulkin, A. Berenguer-Murcia, M. S. Tikhov, B. F. G. Johnson and R. M. Lambert, *Nature*, 2008, **454**, 981–983.
37 A. Nassereddine, Q. Wang, D. Loffreda, C. Ricolleau, D. Alloyeau, C. Louis, L. Delannoy, J. Nelayah and H. Guesmi, *Small*, 2021, **17**, 2104571.
38 Y. Xia, K. D. Gilroy, H.-C. Peng and X. Xia, *Angew. Chem., Int. Ed.*, 2017, **56**, 60–95.
39 A. Gole and C. J. Murphy, *Chem. Mater.*, 2004, **16**, 3633–3640.
40 A. Sánchez-Iglesias and M. Grzelczak, *Small*, 2025, **21**, 2407735.
41 N. Metropolis, A. W. Rosenbluth, M. N. Rosenbluth, A. H. Teller and E. Teller, *J. Chem. Phys.*, 1953, **21**, 1087–1092.
42 V. Rosato, M. Guillope and B. Legrand, *Philos. Mag. A*, 1989, **59**, 321–336.
43 G. Breyton, H. Amara, J. Nelayah, J. Creuze, H. Guesmi, D. Alloyeau, G. Wang and C. Ricolleau, *Phys. Rev. Lett.*, 2023, **130**, 236201.
44 S. Plimpton, *J. Comput. Phys.*, 1995, **117**, 1–19.
45 J. Barthel, *Ultramicroscopy*, 2018, **193**, 1–11.
46 E. J. Kirkland, in *Advanced Computing in Electron Microscopy*, ed. E. J. Kirkland, Springer International Publishing, Cham, 2020, pp. 197–239, DOI: 10.1007/978-3-030-33260-0_7.